


Disentangling electronic, lattice, and spin dynamics in the chiral helimagnet $\text{Cr}_{1/3}\text{NbS}_2$ N. Sirica^{1,2,*}, H. Hedayat,³ D. Bugini³, M. R. Koehler,⁴ L. Li,⁴ D. S. Parker,⁵ D. G. Mandrus,^{4,5,1} C. Dallera,³ E. Carpene⁶, and N. Mannella^{1,†}¹*Department of Physics and Astronomy, The University of Tennessee, Knoxville, Tennessee 37996, USA*²*Center for Integrated Nanotechnologies, Los Alamos National Laboratory, Los Alamos, New Mexico 87545, USA*³*Dipartimento di Fisica, Politecnico di Milano, Piazza Leonardo da Vinci 32, 20133 Milano, Italy*⁴*Department of Materials Science and Engineering, The University of Tennessee, Knoxville, Tennessee 37996, USA*⁵*Materials Science and Technology Division, Oak Ridge National Laboratory, Oak Ridge, Tennessee 37831, USA*⁶*IFN-CNR, Dipartimento di Fisica, Politecnico di Milano, Piazza Leonardo da Vinci 32, 20133 Milano, Italy* (Received 1 April 2021; revised 28 October 2021; accepted 2 November 2021; published 19 November 2021)

We investigate the static and ultrafast magneto-optical response of the hexagonal chiral helimagnet $\text{Cr}_{1/3}\text{NbS}_2$ above and below the helimagnetic ordering temperature. The presence of a magnetic easy plane contained within the crystallographic ab plane is confirmed, while degenerate optical pump-probe experiments reveal significant differences in the dynamic between the parent, NbS_2 , and Cr-intercalated compounds. Time-resolved magneto-optical Kerr effect measurements show a two-step demagnetization process, where an initial, subpicosecond relaxation and subsequent buildup ($\tau > 50\text{ps}$) in the demagnetization dynamic scale similarly with increasing pump fluence. Despite theoretical evidence for partial gapping of the minority spin channel, suggestive of possible half-metallicity in $\text{Cr}_{1/3}\text{NbS}_2$, such a long demagnetization dynamic likely results from spin-lattice relaxation as opposed to minority state blocking. However, comparison of the two-step demagnetization process in $\text{Cr}_{1/3}\text{NbS}_2$ with other $3d$ intercalated transition metal dichalcogenides reveals a behavior that is unexpected from conventional spin-lattice relaxation, and may be attributed to the complicated interaction of local moments with itinerant electrons in this material system.

DOI: [10.1103/PhysRevB.104.174426](https://doi.org/10.1103/PhysRevB.104.174426)**I. INTRODUCTION**

As information storage and processing becomes one of the largest consumers of energy worldwide [1], a need for novel, ultralow power electronics to supersede present day complementary metal-oxide semiconductor (CMOS) devices has emerged. In this regard, many of these next generation electronic devices will rely on the ability to precisely control other intrinsic degrees of freedom (DOF) beyond that of charge. Here, chiral helimagnets (CHMs) have emerged as promising materials to be used for spintronics and other information technologies, where the intent is to actively manipulate either the individual or average spin angular momentum of itinerant carriers [2]. In CHMs the chiral framework of the lattice allows for the arrangement of spins into incommensurate, periodic spirals, or helices, as long as 50 nm in length [3–7], which can collectively host unusual spin textures including two-dimensional spin vortices known as skyrmions [8,9]. Skyrmions are of particular interest in applied technology due to the fact that they can be manipulated, at the nanoscale level, by externally applied magnetic fields [9] and spin polarized currents [10,11], and are found to have a profound influence on electronic transport [12–14].

Given the important functionalities of these materials, there is incentive to discover new CHMs relevant to the design and fabrication of future spintronic devices [15]. One such material is $\text{Cr}_{1/3}\text{NbS}_2$ [16], which has been shown to host a unique one-dimensional solitonic excitation known as a chiral soliton lattice (CSL) [17]. Here, application of a modest ($< 2000\text{Oe}$) magnetic field perpendicular to the helical (c) axis allows for the size of c -axis ferromagnetic domains to be tuned [17]. In this way, the CSL can act as a tunable effective potential for itinerant electron spins, offering the possibility of precisely controlling the transport properties of itinerant spin carriers [18,19]. Furthermore, the high stability and robustness of the CSL phase can pave the way for many new and exciting spintronic functionalities such as spin current induction [20], soliton transport [21], and current driven collective transport [22], all of which have relevance for future technological applications.

Incorporating these materials into future technological devices relies on the ability to manipulate CSL spin textures in a controllable fashion, as well as the speed at which this manipulation takes place. Presently, recording logical bits through writing or erasing domains in magnetic storage devices is limited by the precessional timescale of spins ($\sim 2\text{ps}$) [23,24]. However, through the use of ultrafast magneto-optic effects such as the inverse Faraday effect [25], magnetic DOF can be manipulated on timescales faster than half a precessional period, serving to bridge the ultrafast technology gap through controlling spins on the subpicosecond (sub-ps) timescales of

*nsirica@lanl.gov

†nmannell@utk.edu

the spin-orbit or even exchange interaction [26]. Hence, for CHMs such as $\text{Cr}_{1/3}\text{NbS}_2$, ultrafast magneto-optics opens up the possibility of manipulating magnetic order on ultrashort timescales, as well as studying the coherently excited structural and magnetic dynamics that are unique to this class of materials [27–33].

Recent magnetotransport studies of exfoliated $\text{Cr}_{1/3}\text{NbS}_2$ demonstrate the ability to tune topological indices through transitioning between states having different soliton densities [34]. As with interlayer magnetotransport from bulk crystals [18,19], these measurements reveal a direct correlation between the transverse, negative magnetoresistance and the soliton lattice density, which is attributed to Bragg scattering of conduction electrons by the magnetic superlattice potential of the CSL. While this interplay between macroscopic magnetic and transport DOF is believed to result from a reduction in carrier scattering following spin order, electronic structure measurements taken across the helimagnetic transition reveal a stronger coupling between itinerant electrons and local, Cr-derived magnetic moments [35]. Here, we investigate how such a coupling manifests in the dynamical response through presenting static and transient magneto-optical measurements on $\text{Cr}_{1/3}\text{NbS}_2$ taken above and below the helimagnetic ordering temperature, $T_C = 131$ K. By disentangling the relevant contributions of electron, lattice, and spin from the overall relaxation dynamic, we attribute changes in the electronic and crystalline structure of the parent NbS_2 compound to effects brought on by Cr intercalation. Chief among these includes a sign change in the transient reflectivity that results from the donation of electronic charge into NbS_2 layers by the Cr intercalant, while ultrafast optical excitation generates a coherent, Raman active phonon mode in $\text{Cr}_{1/3}\text{NbS}_2$ that is absent from the parent compound. Finally, time-resolved magneto-optical Kerr effect measurements show an initial, sub-ps relaxation followed by a long (> 30 – 50 ps) buildup in the demagnetization dynamic that scales similarly with increasing pump fluence, pointing towards a predominance of spin-lattice relaxation in the photoinduced demagnetization, though the detailed interaction between local moments and itinerant electrons may make such behavior unconventional. Taken together, these results provide a broad overview of both the static and dynamic magneto-optical properties of this material system.

II. EXPERIMENT

Experiments were performed on as-grown NbS_2 and $\text{Cr}_{1/3}\text{NbS}_2$ single crystals [36], where the latter possesses a $T_C = 131$ K as determined by scanning superconducting quantum interference device (SQUID) magnetometry [35]. Single-crystal growth was carried out under chemical vapor transport using 0.5 g iodine transport agent per 3 g polycrystalline $\text{Cr}_{1/3}\text{NbS}_2$, synthesized by heating stoichiometric ratios of Cr, Nb, and S to 950°C for 1 week. Platelike crystals of $5\text{ mm} \times 5\text{ mm}$ oriented along (001) form across a 100°C (950 – 850°C) temperature gradient of the transport tube. Due to the deleterious effect that Cr disorder has on the appearance of helimagnetism [37], x-ray and low-energy electron diffraction measurements were used to confirm a $P6_322$ space group showing $(\sqrt{3} \times \sqrt{3})R(30^\circ)$ Cr order [36,38], while a

prominent kink in the magnetic susceptibility at $T_C = 131$ K provides indication for helimagnetism in this sample batch [35].

Static magneto-optical Kerr effect (MOKE) measurements obtained under similar experimental conditions as reported in Ref. [39] were taken with a diode laser (< 100 mW) centered at 670 nm (1.85 eV) in a magnetic field (< 500 Oe) applied within both the ab plane and along the noncentrosymmetric c axis. Transient reflectivity from both the paramagnetic and helimagnetic phases of $\text{Cr}_{1/3}\text{NbS}_2$ was measured by an amplified Ti:sapphire laser system operating at 1 kHz repetition rate. Here, ultrashort (~ 50 fs), orthogonally polarized optical pulses centered at either 800 nm (1.55 eV), or employing a supercontinuum probe (450 – 750 nm) generated from a thin sapphire wafer, were incident at $\sim 45^\circ$ with respect to the (001) surface normal of the crystal. In these experiments, a pump fluence of 7.1 mJ/cm^2 was never exceeded. Time-resolved MOKE (trMOKE) measurements were carried out using a noncollinear optical parametric amplifier (NOPA), pumped by a frequency doubled Yb:KGW laser operating at a 100 kHz repetition rate [40,41]. The resultant pulses possess a transform limit of < 30 fs and are centered at $\sim 680\text{ nm}$, so as to match the wavelength used in static MOKE experiments [42].

III. RESULTS AND DISCUSSION

Static MOKE measurements were first performed on $\text{Cr}_{1/3}\text{NbS}_2$ single crystals to quantify the degree of magnetic anisotropy present in this material. Unlike other CHMs, $\text{Cr}_{1/3}\text{NbS}_2$ crystallizes in a more anisotropic layered structure consisting of ferromagnetic planes of Cr atoms intercalated within the van der Waals gaps of NbS_2 layers [43]. Seeing as the Cr atoms host the magnetic moment in this material, such crystalline anisotropy will give rise to a magnetic anisotropy, which can be sensitively detected by MOKE within the $\sim 35\text{ nm}$ optical skin depth probed in our experiment [39]. Figure 1 shows the decomposition of the magnetization vector into three orthogonal directions: transverse, longitudinal, and polar [44]. Here, a large transverse component of the MOKE signal shown in Fig. 1(a) follows from the magnetization aligning parallel to an externally applied, 200 Oe field. For Cr atoms arranging in a $(\sqrt{3} \times \sqrt{3})R(30^\circ)$ superstructure, two in-plane high-symmetry axes can be defined: $\vec{a}_{1,2} = \frac{3}{2}a\hat{x} \pm \frac{\sqrt{3}}{2}a\hat{y}$, where a denotes the in-plane lattice constant of the 1×1 hexagonal unit cell. By measuring MOKE either along these two high-symmetry axes or at 30° with respect to these axes, both of which are known precisely from Laue diffraction, no difference in either the coercive field or peak magnetization was observed. Such insensitivity in the MOKE response to in-plane sample orientation (e.g., azimuthal rotation) indicates there to be no preferred magnetization direction in the ab plane, with the magnetization always aligning parallel to the applied field direction as shown in the inset of Fig. 1(a). Furthermore, by correcting for induction effects through plotting the coercivity with respect to the strength of an applied AC magnetic field, an extrapolation to zero field reveals only a small intrinsic hysteresis present along this axis (Fig. 2). In contrast, Fig. 1(b) shows the polar component of the

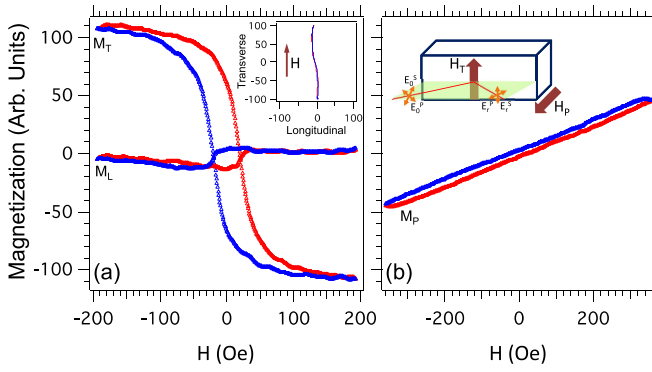


FIG. 1. Decomposition of the magnetization along (a) transverse (M_T), longitudinal (M_L), and (b) polar (M_P) directions as revealed by static magneto-optical Kerr effect (MOKE) measurements. A direct comparison of the transverse and longitudinal MOKE signals shown in the inset of (a) confirms the magnetization in the ab plane to align predominately along the applied field direction. The inset in (b) schematically illustrates the various MOKE geometries as defined by the direction of a transverse (H_T), or polar (H_P) externally applied magnetic field with respect to the scattering plane.

magnetization to be ~ 5 times weaker than that of the transverse component, and to exhibit no saturation despite the use of a stronger applied field. From our MOKE geometry, the noncentrosymmetric c axis is oriented along the polar direction, making such findings consistent with those of Ref. [36], indicating the out of plane direction to be the hard magnetization axis. Taken together with the small intrinsic hysteresis found in the easy (ab) plane, our static MOKE measurements are fully consistent with the bulk magnetization properties of $\text{Cr}_{1/3}\text{NbS}_2$ [36].

Room-temperature transient reflectivity collected from the parent, NbS_2 , and Cr-intercalated compounds following excitation by a $\sim 2.84 \text{ mJ/cm}^2$ optical pump pulse centered at 800 nm (1.55 eV) is shown in Fig. 3. Here, time-dependent traces capturing the relaxation dynamic over short (4.0 ps) and long (50.0 ps) time delays are shown for NbS_2 [Figs. 3(a) and 3(b)]

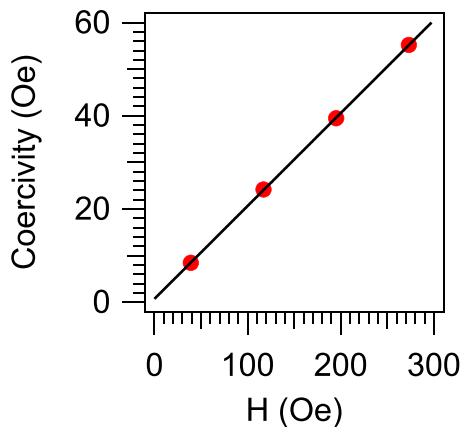


FIG. 2. A plot of the coercivity as a function of field strength for an externally applied AC magnetic field. Extrapolation to zero field allows for induction effects to be corrected, revealing a small intrinsic hysteresis ($0.70642 \pm 0.139 \text{ Oe}$) in this material.

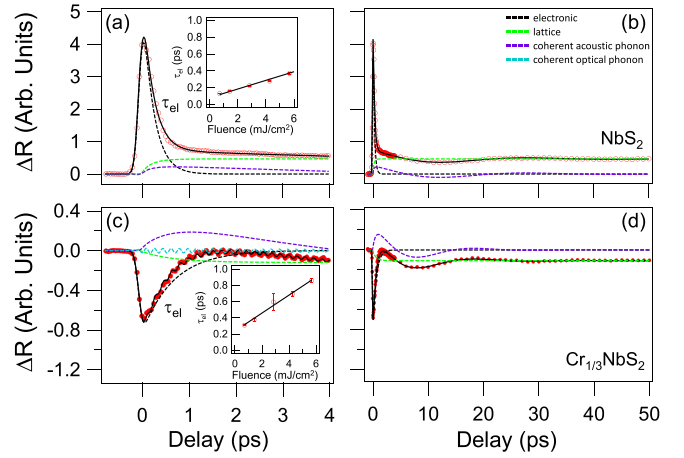


FIG. 3. Room-temperature transient reflectivity spectra of (a,b) NbS_2 and (c,d) $\text{Cr}_{1/3}\text{NbS}_2$ measured over short (4.0 ps) and long (50.0 ps) time delays, following excitation by a 2.84 mJ/cm^2 optical pump pulse. Fits (solid) of the degenerate pump-probe spectra [$\lambda_{\text{pu}} = \lambda_{\text{pr}} = 800 \text{ nm}$ (1.55 eV)] are decomposed into their individual components (dashed) to capture separate electronic, lattice, and coherent phonon dynamics. Insets in (a,c) show a linear scaling to the respective electronic relaxation times, τ_{el} , for NbS_2 and $\text{Cr}_{1/3}\text{NbS}_2$ as a function of pump fluence.

and $\text{Cr}_{1/3}\text{NbS}_2$ [Figs. 3(c) and 3(d)], respectively. In order to capture the overall time resolution of our experiment ($\sigma \sim 70 \text{ fs}$), fits of the transient reflectivity are performed with the use of a phenomenological model described by the convolution of exponential and damped oscillatory decays with a Gaussian excitation pulse, $g(\sigma)$ [45,46].

$$\left[A_{\text{el}} e^{-t/\tau_{\text{el}}} + A_l (1 - e^{-t/\tau_{\text{el}}}) e^{-t/\tau_l} + \sum_{i=1}^2 A_i e^{-t/\tau_i} \cos\left(\frac{2\pi}{T_i} t - \phi_i\right) \right] g(\sigma). \quad (1)$$

Here, time constants τ_{el} and τ_l describe the sub-ps, electronic, and long-lived ($> 50 \text{ ps}$) lattice dynamics, respectively, while $\tau_{i=1,2}$ denote the dephasing times for coherently excited phonon oscillations. Similarly, A_{el} and A_l define the amplitude for the respective electronic and lattice dynamic, while $A_{i=1,2}$, $T_{i=1,2}$, and $\phi_{i=1,2}$ denote the amplitude, period, and initial phase of the coherent phonon modes shown in Figs. 3(b)–3(d), respectively. A comparison of the fit parameters used in Fig. 3 is shown in Table I and is referenced in the discussion below.

A decomposition of the individual fit components is shown in Fig. 3, allowing for specific electronic and lattice dynamics to be isolated. Focusing on the sub-ps electronic relaxation time, τ_{el} , both the parent and Cr-intercalated compounds exhibit a linear scaling in this parameter with increasing pump fluence. Such behavior can be rationalized by an effective temperature (or quasiequilibrium) model, where longer electronic relaxation times result from higher excitation fluences due to a divergence of electronic and lattice temperatures following photoexcitation [47]. The insets in Figs. 3(a) and 3(c) reveal a consistently longer electronic relaxation time for $\text{Cr}_{1/3}\text{NbS}_2$ as compared to NbS_2 , suggesting either a difference in ‘‘hot’’

TABLE I. A comparison of fit parameters for NbS₂ and Cr_{1/3}NbS₂ used in Fig. 3 of the main text. Here, a constant relaxation time, $\tau_l = 1$ ns, was used to describe the long-lived (>50 ps) lattice dynamics present in both the parent and Cr-intercalated compounds as an offset. We note that this dynamic recovers prior to the arrival of the next sequence of light pulses (1 ms) as no evidence of cumulative heating is observed at negative delay (i.e., prior to pump excitation).

	A_{el} (arb. units)	τ_{el} (ps)	A_l (arb. units)	τ_l (ps)	$A_{1=AC}$ (arb. units)	$\tau_{1=AC}$ (ps)	$T_{1=AC}$ (ps)	$\phi_{1=AC}$	$A_{2=OP}$ (arb. units)	$\tau_{2=OP}$ (ps)	$T_{2=OP}$ (ps)	$\phi_{2=OP}$ (ps)
NbS ₂	4.7×10^{-2}	0.22	3.1×10^{-3}	1000	8.8×10^{-4}	13.6	26.8	-0.01	–	–	–	–
Cr _{1/3} NbS ₂	-6.3×10^{-3}	0.60	-7.4×10^{-4}	1000	8.8×10^{-4}	6.9	20.5	0.23	8.6×10^{-5}	6.6	0.17	0.25

electron transport, or that Cr intercalation leads to a weaker coupling between electronic and lattice DOF. This latter claim is rooted in the fact that a “hot” population of transiently excited electrons can decay through an exchange of energy with the lattice. Here, a lower Debye temperature (T_D) for NbS₂ (260 K [48]) as compared to Cr_{1/3}NbS₂ (419 K [36]) implies the full phonon spectrum is excited within the parent, NbS₂, compound at the experimental temperature of 300 K. This results in a faster electronic relaxation in the parent compound due to a more efficient energy exchange between electronic and lattice DOF, provided by an increased density of available phonon states for $T > T_D$.

Aside from this comparison of the electronic relaxation time, the most prominent difference between the transient reflectivity for the parent and Cr-intercalated compounds in Fig. 3 is a sign change in the dynamic. Use of a broadband probe shows an opposing sign for the dynamical response of NbS₂ and Cr_{1/3}NbS₂ to exist over a wide wavelength range, with a clear reversal occurring between 600 and 650 nm (1.91–2.07 eV) as shown in Fig. 4. Such behavior has been observed in other 3d intercalated transition metal dichalcogenides (TMDs) [30], suggesting it to be a generic effect attributed to a shift in the chemical potential that accompanies the donation of electronic charge to NbS₂ layers following

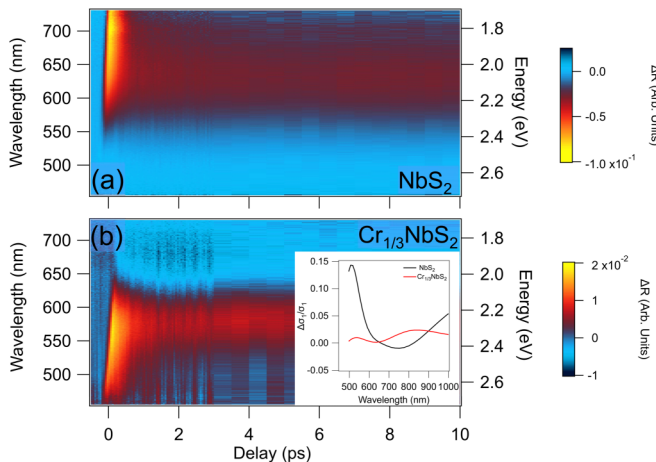


FIG. 4. Transient reflectivity of (a) NbS₂ and (b) Cr_{1/3}NbS₂ measured by a broadband optical probe ($\lambda_{pr} \sim 450$ –750 nm) following 800 nm pump excitation ($F = 2.84$ mJ/cm²). Inset shows the calculated (see the Appendix) change in the real part of the optical conductivity for NbS₂ and Cr_{1/3}NbS₂ as a function of photon energy. A sign reversal of the dynamic at $\lambda_{pr} \sim 600$ –650 nm is captured by an effective temperature model and is owed to the shift in chemical potential that accompanies Cr intercalation.

intercalation [38]. Considering a linear scaling for the fluence dependence of the electronic relaxation time to be well characterized by an effective temperature model, the transient optical response can be described as a predominately thermal effect by computing the real part of the optical conductivity, $\sigma_1(\omega)$, at electronic temperatures $T_1 = 300$ K and $T_2 = 1200$ K (Appendix). Here, a key difference in the real part of $\sigma_1(\omega)$ between NbS₂ and Cr_{1/3}NbS₂ is the effect of electron doping from the intercalant on the joint density of states. A calculation of the relative variation in $\Delta\sigma_1/\sigma_1 = \sigma_1(T_2)/\sigma_1(T_1) - 1$, accounting for such doping effects, captures the sign difference in the dynamic over the same probe wavelength range experimentally observed, as shown in the inset of Fig. 4(b). Such a calculation thus provides a physical rationale for this sign change in the transient reflectivity to result from Cr-induced electron doping in the electronic structure of the parent NbS₂ compound.

In addition to modifying the electronic structure, intercalation leads to a Raman active lattice vibration that is absent from the parent compound [Fig. 3(c)]. Here, the coherent generation of optical phonons following nonresonant, ultrafast photoexcitation can occur through a displacive excitation in which optical pumping suddenly shifts the vibrational potential minimum [49], or by an impulsively stimulated Raman process, where the broad bandwidth of an ultrashort laser pulse yields multiple combinations of two photon difference frequencies required for stimulated Raman scattering [50]. Noting vibrational modes to be constrained by lattice symmetry, the D_{6h} point group of NbS₂ supports four Raman active phonon modes: A_{1g} , E_{1g} , E_{2g}^1 , and E_{2g}^2 . With the exception of the E_{2g}^2 rigid layer mode, these phonon modes are at considerably higher energies [51], and thus faster timescales, to be resolved in our experiment, while the coherent excitation of the weaker E_{2g}^2 mode at 0.93 THz is absent from both the NbS₂ and Cr_{1/3}NbS₂ transient reflectivity spectra. Fits of the oscillatory dynamic in Cr_{1/3}NbS₂ reveal a dominant single mode at 5.75 THz having a dephasing time of ~ 7 ps (Fig. 5), indicative of a comparatively long phonon lifetime [52]. Here, the dynamic shows no dependence on pump polarization, or softening with increasing pump fluence, suggesting the interatomic potential to be robust against optical excitation. Coupled with the fact that this coherently excited phonon mode is unique to the Cr-intercalated compound, such behavior is consistent with an intralayer, intercalant phonon as reported in Ref. [53].

While the coherent excitation of an optical, intralayer intercalant mode in Fig. 3(c) is assumed to be impulsive in nature, the generation of longitudinal acoustic (LA) phonons in Figs. 3(b) and 3(d) results from strain wave propagation

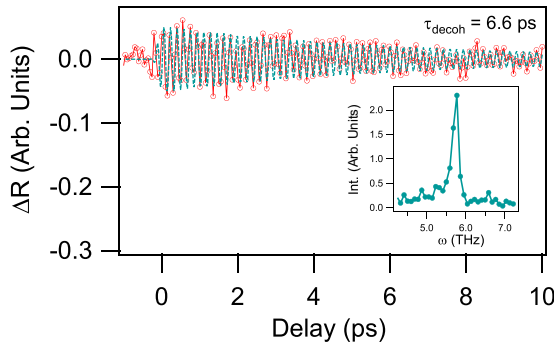


FIG. 5. Isolated oscillatory dynamic from the transient reflectivity of $\text{Cr}_{1/3}\text{NbS}_2$ obtained at room temperature following excitation by a 2.84 mJ/cm^2 optical pump pulse centered at $\lambda_{\text{pu}} = \lambda_{\text{pr}} = 800 \text{ nm}$ (1.55 eV). Fit to the dynamic of the intercalant phonon mode reveals a 5.75 THz frequency (inset) showing a 6.6 ps decoherence time.

along the surface normal of NbS_2 and $\text{Cr}_{1/3}\text{NbS}_2$ respectively, and forms in response to an external stress introduced by the laser pulse. Microscopically, such a strain wave can arise from thermoelastic or piezoelectric effects, as well as electron phonon coupling, driven by the excitation of photocarriers [54–56]. Discerning the exact microscopic mechanism for LA mode generation following optical excitation is beyond the scope of this work, but the minimum timescale for the onset of LA dynamics should be determined by electronic relaxation in much the same way as the lattice dynamic in Eq. (1). Thus, our phenomenological fit model used to capture these coherently excited acoustic modes is similarly coupled to the electronic relaxation time. However, such a sub-ps rise time has little influence on the overall dynamic of these low-frequency phonon modes, which themselves do not significantly affect the dynamical properties of the electronic and spin DOF in these compounds.

The transient reflectivities measured above and below the helimagnetic transition temperature are compared in Fig. 6. Here, a similar electronic and lattice dynamic is seen for the paramagnetic and helimagnetic phase, with both exhibiting an initial electronic excitation that recovers over a sub-ps timescale, as well as the coherent generation of an acoustic strain wave, showing no change in frequency or dampening as temperature is lowered from 300 to 80 K . A 0.3 THz oscillation is observed in both the paramagnetic and helimagnetic phase of Fig. 6, ruling out any spin-wave dynamic, suggesting instead a lattice dynamic resulting from a low-frequency, interlayer breathing or shear mode, as commonly seen in layered TMDs [57]. As compared to Fig. 6(a), an increase in the offset ($>50 \text{ ps}$) for the time trace shown in Fig. 6(b) follows from the reduced specific heat of the crystal, accompanying a marked drop in temperature below T_D (i.e., $T \ll T_D$), leading to increased lattice heating under optical excitation. In contrast, an additional, nontrivial dynamic is shown in the helimagnetic phase [Fig. 6(b)], which is captured by an exponential rise, $A_R(1 - e^{-t/\tau_R})g(\sigma)$, having a considerably longer timescale, $\tau_r > 50 \text{ ps}$, than the electronic and lattice dynamic found in the paramagnetic phase. This is attributed to a demagnetization dynamic, which emerges within the

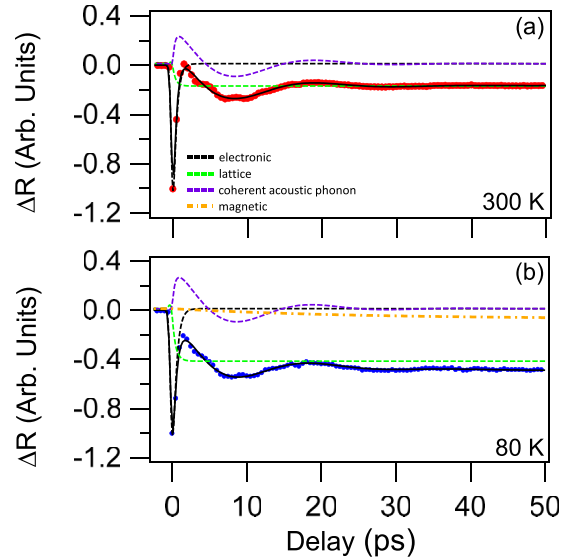


FIG. 6. Transient reflectivity measured from $\text{Cr}_{1/3}\text{NbS}_2$ in the (a) paramagnetic (300 K) and (b) helimagnetic (80 K) phases using $\lambda_{\text{pu}} = \lambda_{\text{pr}} = 800 \text{ nm}$ (1.55 eV) under a pump fluence of 3.0 mJ/cm^2 . Fits shown as solid traces are decomposed into their separate dynamical components (dashed), where similar electronic, lattice, and coherent phonon dynamics are seen in both the paramagnetic and helimagnetic phase, while a long demagnetization dynamic develops in the helimagnetic phase for $T < T_C$.

transient reflectivity at temperatures below the helimagnetic transition temperature under increasing excitation fluence (Fig. 7).

Such a magnetic dynamic can be isolated through the use of trMOKE, where photoinduced demagnetization over short ($< 3 \text{ ps}$) and long ($> 250 \text{ ps}$) time delays is illustrated in Fig. 8. Here, trMOKE traces shown as a function of increasing pump fluence exhibit both an initial, sub-ps relaxation ($\tau_{M1} = 0.26 \text{ ps}$ to $\tau_{M1} = 0.42 \text{ ps}$) and subsequent buildup ($\tau_{M2} = 28 \text{ ps}$ to $\tau_{M2} = 53 \text{ ps}$) within the demagnetization dynamic that scale similarly with increasing pump fluence (Fig. 8 inset). Both optical pump-probe and trMOKE measurements yield nearly identical rise times for this long demagnetization dynamic for $T < T_C$ (Fig. 9). However, the relative variation of the intensity-dependent (optical), versus polarization-dependent (Kerr), probe is three orders of magnitude smaller, indicating a comparatively weak optical contribution to the trMOKE response.

In contrast, the initial ultrafast dynamic, depicted as an inset in Fig. 9, reveals a distinct relaxation dynamic for trMOKE ($\tau_{M1} = 0.4 \text{ ps} \pm 0.07 \text{ ps}$) as compared to transient reflectivity ($\tau_{el} = 0.32 \text{ ps} \pm 0.02 \text{ ps}$) experiments. This behavior is expected due to the predominance of an electronic, rather than magnetic, response governing the relaxation dynamic measured by optical pump-probe over ultrashort timescales. Consequently, the photoinduced demagnetization in $\text{Cr}_{1/3}\text{NbS}_2$ can be defined over two dominant timescales: an ultrafast demagnetization directly affected by optical excitation, and a slow buildup in the demagnetization dynamic occurring over timescales that extend beyond the initial electronic relaxation.

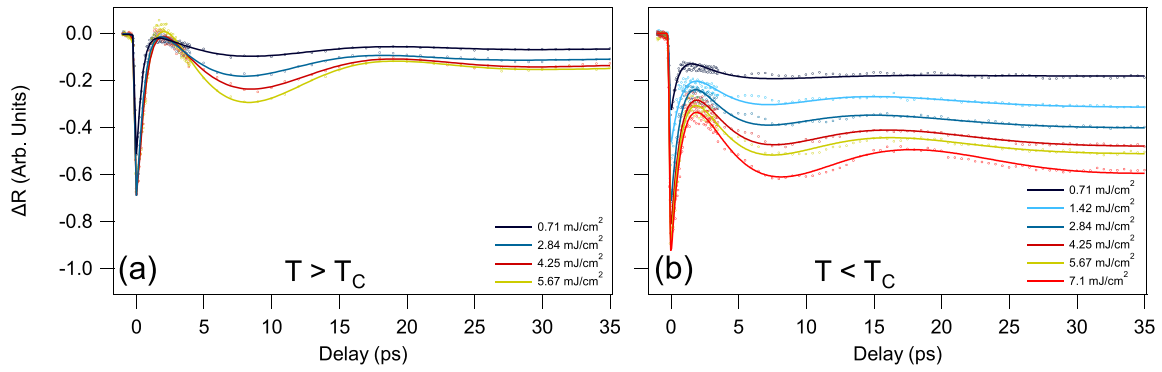


FIG. 7. (a) High ($T > T_C$; 300 K) and (b) low ($T < T_C$; 80 K) temperature, fluence dependence ($\lambda = 800$ nm; $h\nu = 1.55$ eV) measured from $\text{Cr}_{1/3}\text{NbS}_2$ showing an emergent magnetic dynamic at temperatures below the helimagnetic transition with increasing excitation fluence.

A central question surrounding photoinduced demagnetization is where and on what timescale is angular momentum being transferred from the spin subsystem. On the one hand, angular momentum can be retained entirely by the spins and demagnetization results from the rapid transport of spin majority carriers out of the probe volume [58]. However, such superdiffusive transport can explain a sub-ps demagnetization, such as the one shown in Fig. 8(a), only in metallic systems having high-mobility, itinerant spin carriers, which contrasts with the poor electronic transport properties exhibited by $\text{Cr}_{1/3}\text{NbS}_2$ [36]. On the other hand, a transfer of spin angular momentum to the lattice can follow from either spin-wave (magnon) excitations [59], or more directly through phonon mediated spin-flip scattering [60,61], which itself can result in the emission of phonons through an ultrafast Einstein–de Haas effect [62]. Such a phonon mediated scattering process, known as the Elliott–Yafet mechanism, describes single-particle, spin-flip scattering from an impurity or phonon that is attributed to band mixing of spin-up and spin-down states arising from the spin-orbit interaction [63,64]. This process results in a transient population of unoccupied, minority spin states following photoexcitation. However, an opening of this spin-flip scattering channel requires a suffi-

cient density of minority spin states in proximity to the Fermi level (E_F) to be available, which may not be the case for $\text{Cr}_{1/3}\text{NbS}_2$.

Depending on the position of the chemical potential relative to the valence band maximum of minority spin states, a spin-flip scattering process can be inhibited when significantly fewer states are present in the minority spin channel, blocking the energy transfer between the electronic and spin DOF. This occurrence is commonly referred to as minority state blocking, and results in an situation analogous to that of magnetic dielectrics, where energy transfer occurs directly through the lattice by way of spin-lattice relaxation [65,66]. Since the lattice and spin DOF are weakly coupled, this can give rise to a characteristically long demagnetization dynamic that scales inversely with $(1-P_n)$, for P_n denoting the degree of spin polarization present in the magnetic phase, making such a long dynamic a defining signature for some half-metals [67]. Spin-polarized *ab initio* calculations for $\text{Cr}_{1/3}\text{NbS}_2$ [38,68] suggest

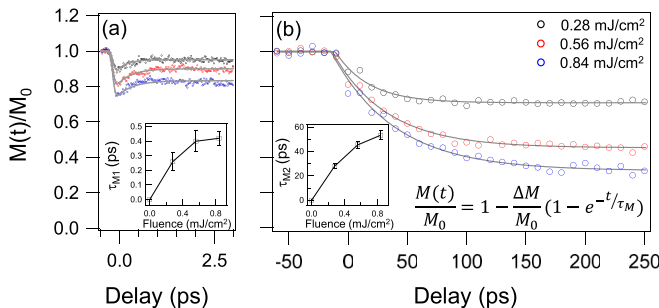


FIG. 8. Photoinduced demagnetization of $\text{Cr}_{1/3}\text{NbS}_2$ measured over (a) short (< 3 ps) and (b) long (> 250 ps) time delays by time-resolved, transverse MOKE in the helimagnetic phase ($T = 80$ K) as a function of increasing pump fluence (0.28–0.84 mJ/cm^2). Fits shown as solid gray lines follow a phenomenological model described by two demagnetization time constants, $\tau_{M1,2}$, sharing a similar dependence on pump fluence as illustrated in the inset.

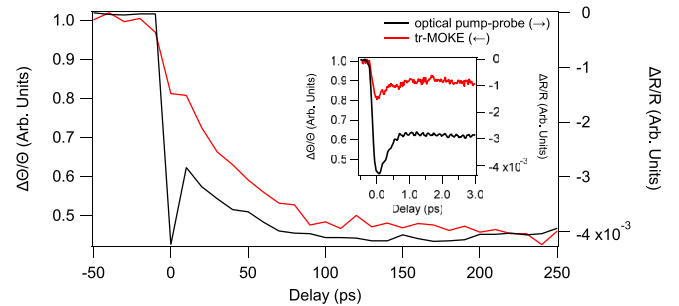


FIG. 9. Overlay of optical pump-probe (black) and trMOKE (red) traces measured in the helimagnetic phase under a 0.58 mJ/cm^2 pump excitation centered at 680 nm (1.82 eV). Both transient reflectivity and trMOKE show a similar magnetic dynamic over long ($\tau_{M2} = 45.4$ ps and $\tau_{M2} = 43.7$ ps, respectively) timescales, while a relative variation of more than three orders of magnitude is seen between the optical and Kerr responses. Inspection of the initial ultrafast dynamic (inset) reveals a distinct relaxation dynamic for trMOKE ($\tau_{M1} = 0.4 \pm 0.07$ ps) as compared to transient reflectivity ($\tau = 0.32 \pm 0.02$ ps). This behavior is expected due to the predominance of an electronic, as opposed to magnetic, response governing the relaxation dynamic from optical pump-probe over ultrashort timescales.

this material to be half-metallic, where the presence of a narrow gap (<100 meV) in the minority spin channel leads to the suppression of interlayer transport, a reduced dimensionality of the electronic structure, and an increased anisotropy in the majority spin channel [38]. However, the magnetic dynamic shown in Fig. 8 not only shows a long buildup in the demagnetization, characterized by an exponential rise τ_{M2} , but also an ultrafast component, τ_{M1} , whose relaxation occurs over a sub-ps timescale. Similar to half-metallic Heusler alloys, where the photon energy can exceed the band gap of the minority spin channel by orders of magnitude, the presence of a slow demagnetization dynamic alone is not a universal characteristic of all half-metals, as the efficiency of optical excitation for majority and minority carriers, hole dynamics below E_F , and conduction band bandwidth can all influence the photoinduced demagnetization [69–71].

Rather, a monotonic increase of this long demagnetization time constant τ_{M2} with pump fluence likely reflects a weakened magnetic anisotropy, resulting from an increase in lattice temperature brought on by higher excitation density, as opposed to minority state blocking. While this scenario is consistent with spin-lattice relaxation [65,66], it is interesting to note that a corresponding two-step demagnetization process has been observed in related $3d$ intercalated TMDs, where remarkably similar dynamics were found despite a difference in orbital moment, and thus magnetic anisotropy, of the intercalant ion [30]. This is unexpected for a conventional spin-lattice relaxation mechanism, in which deviation away from such conventional behavior is attributed to the detailed interaction between local moments and itinerant electrons present in these material systems. Such findings agree with recent photoemission results, as the presence of hybridized Nb- and Cr-derived states at E_F implies a clear separation between magnetic and itinerant states is untenable, with the same states participating in the formation of the moment likewise participating in the formation of the Fermi surface [35]. Ultimately, more detailed studies directly measuring how the spin-polarized electronic structure can influence the magnetic dynamic in this class of materials are needed, especially as it pertains to possible half-metallicity in $\text{Cr}_{1/3}\text{NbS}_2$ [72].

In closing, we performed a series of static and time-resolved magneto-optical measurements on the chiral helimagnet $\text{Cr}_{1/3}\text{NbS}_2$, with the aim of disentangling the relevant contributions arising from electron, lattice, and spin from the overall relaxation dynamics. Static MOKE supports the fact that $\text{Cr}_{1/3}\text{NbS}_2$ possesses a magnetic easy plane with the c axis being the hard magnetization axis. A comparison of transient reflectivity taken from $\text{Cr}_{1/3}\text{NbS}_2$ in the paramagnetic state with its parent compound NbS_2 reveals several differences that can be attributed to changes in the electronic and lattice structure arising from Cr intercalation. Chief among these is a difference of sign in the dynamic resulting from a change in optical conductivity brought on by the donation of electronic charge into NbS_2 layers following intercalation. In the magnetic phase, time-resolved magneto-optical Kerr effect measurements show an initial, sub-ps relaxation followed by a long (> 30 – 50 ps) buildup in the demagnetization dynamic that scales similarly with increasing pump fluence. Despite

evidence for partial gapping of the minority spin channel, suggestive of possible half-metallicity in $\text{Cr}_{1/3}\text{NbS}_2$, such a long demagnetization dynamic may not be characteristic of minority state blocking, but rather points to the predominance of a spin-lattice relaxation pathway. However, the similarity of this two-step demagnetization process in $\text{Cr}_{1/3}\text{NbS}_2$ with other $3d$ intercalated TMDs having different orbital moments, and thus magnetic anisotropies, is unexpected for conventional spin-lattice relaxation, and may be attributed to the complicated interaction of local moments with itinerant electrons in these material systems. This work suggests that the details of the electronic structure can be important for a correct interpretation of the magneto-optical response in this class of materials. While electronic structure measurements taken across the helimagnetic transition show a strong coupling between itinerant electrons and local, Cr-derived magnetic moments, more detailed studies directly measuring how the spin-polarized electronic structure can influence the magnetic dynamic in this class of materials are needed.

ACKNOWLEDGMENTS

This work was supported by the National Science Foundation, Division of Material Research, Grant No. DMR-1151687. N.S. would like to thank Ra'anam I. Tobey for the helpful discussions. N.S. acknowledges the support of the U.S. Department of Energy through the LANL LDRD Program and the Center for Integrated Nanotechnologies at Los Alamos National Laboratory (LANL), a U.S. Department of Energy, Office of Basic Energy Science user facility. Work at Oak Ridge National Laboratory (ORNL) was supported by the U.S. Department of Energy (DOE), Office of Science, Basic Energy Sciences, Materials Science and Engineering Division. D.M. acknowledges support from the Gordon and Betty Moore Foundation's EPiQS Initiative, Grant No. GBMF9069.

APPENDIX

1. Determination of $\Delta\sigma_1$

Optical pump-probe spectroscopy measures a change in optical reflectivity brought on by an initial, ultrafast, optical excitation. Given the reflectivity to be expressed as a function of the complex refractive index, $\tilde{n}(\omega)$, for ω denoting the frequency, and therefore photon energy, any change in reflectivity can be captured by a change in \tilde{n} for a fixed angle of incidence. Relating this change in \tilde{n} to details of the electronic structure, like the joint density of states, can be approximated through an estimation of the real part of the optical conductivity, σ_1 , from band structure calculations. Specifically, for $\tilde{n}^2 = \epsilon_1 + i\epsilon_2 = 1 + i\frac{4\pi}{\omega}(\sigma_1 + i\sigma_2)$ [73], where $\epsilon_{1,2}$ denotes the respective real and imaginary components of the complex dielectric function, a determination of $\sigma_1 \propto \epsilon_2$ can be calculated from Fermi's "golden rule" as [74]

$$\sigma_1(\omega) \propto \sum_{ij} f |\langle i, k | p | j, k \rangle|^2 \delta(E_j - E_i - \hbar\omega) dk, \quad (\text{A1})$$

where $\sigma_2 \propto \epsilon_1$ can be obtained via Kramers-Kronig relations. Assuming the matrix elements describing a dipole transition

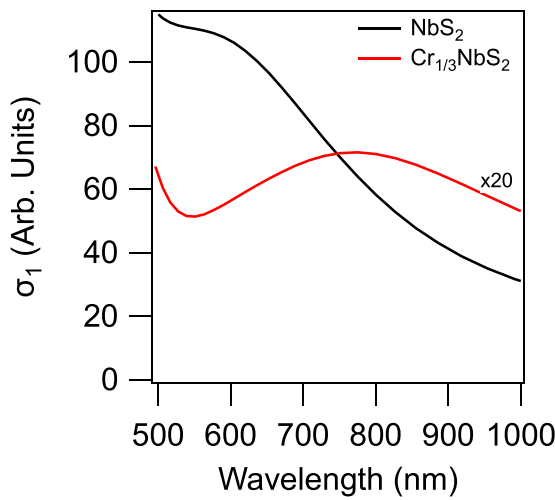


FIG. 10. Calculated real part of the optical conductivity, σ_1 , for NbS_2 and $\text{Cr}_{1/3}\text{NbS}_2$ ($\times 20$) shown as a function of wavelength.

between initial $|i\rangle$, and final $|j\rangle$, states to be constant, this expression for Eq. (A1) reduces to a measure of the joint density of states (JDOS). Accounting for finite temperature through the introduction of a Fermi-Dirac distribution $f(E, T)$ allows for an increase in the effective electronic temperature

T , brought on by optical pumping to be estimated as

$$\sigma_1(\omega, T) \propto \text{JDOS} \propto \int_{E_F - \hbar\omega}^{E_F} \text{DOS}(E) f(E, T) \text{DOS}(E + \hbar\omega) \times [1 - f(E + \hbar\omega, T)] dE. \quad (\text{A2})$$

Using the calculated density of states from NbS_2 [75] and $\text{Cr}_{1/3}\text{NbS}_2$ [76], where changes in the latter reflect a shift in chemical potential brought on by Cr intercalation [38], Fig. 10 shows the computed JDOS at room temperature, which has been smoothed to better match experimental conditions arising from the broadband excitation of an ultrashort laser pulse. In the simplest case, photoexcitation raises the electronic temperature, leading to a transient change in the optical conductivity defined by $\Delta\sigma_1/\sigma_1 = \sigma_1(T_2)/\sigma_1(T_1) - 1$. Setting $T_2 = 1200$ K and $T_1 = 300$ K in the computation of $\Delta\sigma_1/\sigma_1$ (Fig. 4, inset) provides a simple picture for the observed sign change in the experimental data, which is based entirely on changes to the JDOS resulting from the donation of electronic charge into NbS_2 layers following Cr intercalation. We emphasize that such behavior is generic, as a similar sign change is observed in other $3d$ intercalated transition metal dichalcogenides [30], suggesting our simplified model captures the fundamental physics underlying transient reflectivity in these material systems.

- [1] A. Shehabi, S. Smith, D. Sartor, R. Brown, M. Herrlin, J. Koomey, E. R. Masanet, N. Horner, I. Azevedo, and W. Lintner, United States Data Center Energy Usage Report (Lawrence Berkeley National Laboratory, Berkeley, California, 2016).
- [2] I. Zutic, J. Fabian, and S. Das Sarma, Spintronics: Fundamentals and applications, *Rev. Mod. Phys.* **76**, 323 (2004)
- [3] Y. Ishikawa, K. Tajima, D. Bloch, and M. Roth, Helical spin structure in manganese silicide MnSi , *Solid State Commun.* **19**, 525 (1976).
- [4] S. V. Grigoriev, D. Chernyshov, V. A. Dyadkin, V. Dmitriev, S. V. Maleyev, E. V. Moskvina, D. Menzel, J. Schoenes, and H. Eckerlebe, Crystal Handedness and Spin Helix Chirality in $\text{Fe}_{1-x}\text{Co}_x\text{Si}$, *Phys. Rev. Lett.* **102**, 037204 (2009).
- [5] T. Moriya and T. Miyadai, Evidence for the helical spin structure due to antisymmetric exchange interaction in $\text{Cr}_{1/3}\text{NbS}_2$, *Solid State Commun.* **42**, 209 (1982).
- [6] Y. Kousaka, H. Ohsumi, T. Komesu, T.-h. Arima, M. Takata, S. Sakai, M. Akita, K. Inoue, T. Yokobori, Y. Nakao, and E. Kaya, Crystallographic chirality of CsCuCl_3 probed by resonant circularly-polarized hard x-ray diffraction, *J. Phys. Soc. Jpn.* **78**, 123601 (2009).
- [7] K. Ionoue, K. Kikuchi, M. Ohba, and K. Okawa, Structure and magnetic properties of a chiral two-dimensional ferrimagnet with T_C of 38 K, *Angew. Chem., Int. Ed.* **42**, 4810 (2003).
- [8] N. Nagaosa and Y. Tokura, Topological properties and dynamics of magnetic skyrmions, *Nat. Nanotechnol.* **8**, 899 (2013).
- [9] U. K. Rößler, A. N. Bogdanov, and C. Pfleiderer, Spontaneous skyrmion ground state in magnetic metals, *Nature (London)* **442**, 797 (2006).
- [10] F. Jonietz, S. Mühlbauer, C. Pfleiderer, A. Neubauer, W. Münzer, A. Bauer, T. Adams, R. Georgii, P. Böni, R. A. Duim, K. Everschor, M. Garst, and A. Rosch, Spin transfer torques in MnSi at ultralow current densities, *Science* **330**, 1648 (2010).
- [11] N. Romming, C. Hanneken, M. Menzel, J. E. Bickel, B. Wolter, K. von Bergmann, A. Kubetzka, and R. Wiesendanger, Writing and deleting single magnetic skyrmions, *Science* **341**, 636 (2013).
- [12] C. Pfleiderer and A. Rosch, Condensed-matter physics: Single skyrmions spotted, *Nature (London)* **465**, 880 (2010).
- [13] M. Lee, W. Kang, Y. Onose, Y. Tokura, and N. Ong, Unusual Hall Effect Anomaly in MnSi under Pressure, *Phys. Rev. Lett.* **102**, 186601 (2009).
- [14] A. Neubauer, C. Pfleiderer, B. Binz, A. Rosch, R. Ritz, P. Niklowitz, and P. Böni, Topological Hall Effect in the A Phase of MnSi , *Phys. Rev. Lett.* **102**, 186602 (2009).
- [15] N. Kiselev and A. Bogdanov, Chiral skyrmions in thin magnetic films: New objects for magnetic storage technologies?, *J. Phys. D: Appl. Phys.* **44**, 392001 (2011).
- [16] T. Miyadai, K. Kikuchi, H. Kondo, S. Sakka, M. Arai, and Y. Ishikawa, Magnetic properties of $\text{Cr}_{1/3}\text{NbS}_2$, *J. Phys. Soc. Jpn.* **52**, 1394 (1983).
- [17] Y. Togawa, T. Koyama, K. Takayanagi, S. Mori, Y. Kousaka, J. Akimitsu, S. Nishihara, K. Inoue, A. Ovchinnikov, and J. Kishine, Chiral Magnetic Soliton Lattice on a Chiral Helimagnet, *Phys. Rev. Lett.* **108**, 107202 (2012).
- [18] J. Kishine, I. V. Proskurin, and A. S. Ovchinnikov, Tuning Magnetotransport through a Magnetic Kink Crystal in a Chiral Helimagnet, *Phys. Rev. Lett.* **107**, 017205 (2011).

- [19] Y. Togawa, Y. Kousaka, S. Nishihara, K. Inoue, J. Akimitsu, A. S. Ovchinnikov, and J. Kishine, Interlayer Magnetoresistance due to Chiral Soliton Lattice Formation in Hexagonal Chiral Magnet CrNb_3S_6 , *Phys. Rev. Lett.* **111**, 197204 (2013).
- [20] I. Bostrem, J. Kishine, and A. Ovchinnikov, Transport spin current driven by the moving kink crystal in a chiral helimagnet, *Phys. Rev. B* **77**, 132405 (2008).
- [21] A. Borisov, J. Kishine, I. Bostrem, and A. Ovchinnikov, Magnetic soliton transport over topological spin texture in chiral helimagnet with strong easy-plane anisotropy, *Phys. Rev. B* **79**, 134436 (2009).
- [22] J. Kishine, A. Ovchinnikov, and I. Proskurin, Sliding conductivity of a magnetic kink crystal in a chiral helimagnet, *Phys. Rev. B* **82**, 064407 (2010).
- [23] Th. Gerrits, H. A. M. van den Berg, J. Hohlfeld, L. Bar, and Th. Rasing, Ultrafast precessional magnetization reversal by picosecond magnetic field pulse shaping, *Nature (London)* **418**, 509 (2002).
- [24] I. Tudosa, C. Stamm, A. B. Kashuba, F. King, H. C. Siegmann, J. Stohr, G. Ju, B. Lu, and D. Weller, The ultimate speed of magnetic switching in granular recording media, *Nature (London)* **428**, 831 (2004).
- [25] A. V. Kimel, A. Kirilyuk, P. A. Usachev, R. V. Pisarev, A. M. Balbashov, and Th. Rasing, Ultrafast non-thermal control of magnetization by instantaneous photomagnetic pulses, *Nature (London)* **435**, 655 (2005).
- [26] A. Kirilyuk, A. V. Kimel, and Th. Rasing, Ultrafast optical manipulation of magnetic order, *Rev. Mod. Phys.* **82**, 2731 (2010).
- [27] J. D. Koralek, D. Meier, J. P. Hinton, A. Bauer, S. A. Parameswaran, A. Vishwanath, R. Ramesh, R. W. Schoenlein, C. Pfleiderer, and J. Orenstein, Observation of Coherent Helimagnons and Gilbert Damping in an Itinerant Magnet, *Phys. Rev. Lett.* **109**, 247204 (2012).
- [28] T. Schwarze, J. Waizner, M. Garst, A. Bauer, I. Stasinopoulos, H. Berger, C. Pfleiderer, and D. Grundler, Universal helimagnon and skyrmion excitations in metallic, semiconducting and insulating chiral magnets, *Nat. Mater.* **14**, 478 (2015).
- [29] M. Kataoka, Spin waves in systems with long period helical spin density waves due to the antisymmetric and symmetric exchange interaction, *J. Phys. Soc. Jpn.* **56**, 3635 (1987).
- [30] Q. Liu, X. D. Zhu, L. H. Wang, S.-W. Cheong, and R. I. Tobey, Ultrafast magnetization and structural dynamics in the intercalated transition metal dichalcogenides $\text{Fe}_{0.25}\text{TaS}_2$ and $\text{Mn}_{0.25}\text{TaS}_2$, *J. Phys.: Condens. Matter* **28**, 194002 (2016).
- [31] Th. Danz, Q. Liu, X. D. Zhu, L. H. Wang, S.-W. Cheong, I. Radu, C. Ropers, and R. I. Tobey, Structural and magnetic characterization of large area, free standing thin films of magnetic ion intercalated dichalcogenides $\text{Mn}_{0.25}\text{TaS}_2$ and $\text{Fe}_{0.25}\text{TaS}_2$, *J. Phys.: Condens. Matter* **28**, 356002 (2016).
- [32] N. L. Nair, E. Maniv, C. John, S. Doyle, J. Orenstein, and J. G. Analytis, Electrical switching in a magnetically intercalated transition metal dichalcogenide, *Nat. Mater.* **19**, 153 (2020).
- [33] A. Little, C. Lee, C. John, S. Doyle, E. Maniv, N. Nair, W. Chen, D. Rees, J. W. F. Venderbos, R. M. Fernandes, J. G. Analytis, and J. Orenstein, Three-state nematicity in the triangular lattice antiferromagnet $\text{Fe}_{1/3}\text{NbS}_2$, *Nat. Mater.* **19**, 1062 (2020).
- [34] L. Wang, N. Chepiga, D.-K. Ki, L. Li, F. Li, W. Zhu, Y. Kato, O. S. Ovchinnikova, F. Mila, I. Martin, D. Mandrus, and A. F. Morpurgo, Controlling the Topological Sector of Magnetic Solitons in Exfoliated $\text{Cr}_{1/3}\text{NbS}_2$ Crystals, *Phys. Rev. Lett.* **118**, 257203 (2017).
- [35] N. Sirica, P. Vilmercati, F. Bondino, I. Pis, S. Nappini, S.-K. Mo, A. V. Federov, P. K. Das, I. Vobornik, J. Fujii, L. Li, D. Sapkota, D. S. Parker, D. G. Mandrus, and N. Mannella, The nature of ferromagnetism in the chiral helimagnet $\text{Cr}_{1/3}\text{NbS}_2$, *Commun. Phys.* **3**, 65 (2020).
- [36] N. J. Ghimire, M. A. McGuire, D. S. Parker, B. Sipos, S. Tang, J.-Q. Yan, B. C. Sales, and D. Mandrus, Magnetic phase transitions in single crystals of the chiral helimagnet $\text{Cr}_{1/3}\text{NbS}_2$, *Phys. Rev. B* **87**, 104403 (2013).
- [37] V. Dayadkin, F. Mushenok, A. Basak, D. Menzel, S. Grigoriev, P. Pattison, and D. Chernyshov, Structural disorder versus chiral magnetism in $\text{Cr}_{1/3}\text{NbS}_2$, *Phys. Rev. B* **91**, 184205 (2015).
- [38] N. Sirica, S.-K. Mo, F. Bondino, I. Pis, S. Nappini, P. Vilmercati, J. Yi, Z. Gai, P. C. Snijders, P. Das, I. Vobornik, N. Ghimire, M. R. Koehler, D. Sapkota, D. Parker, D. G. Mandrus, and N. Mannella, Electronic structure of the chiral helimagnet and $3d$ intercalated transition metal dichalcogenide $\text{Cr}_{1/3}\text{NbS}_2$, *Phys. Rev. B* **94**, 075141 (2016).
- [39] E. Carpena, E. Mancini, C. Dellera, E. Puppini, and S. De Silvestri, Three-dimensional magnetization evolution and the role of anisotropies in thin Fe/MgO films: Static and dynamic measurements, *J. Appl. Phys.* **108**, 063919 (2010).
- [40] F. Boschini, H. Hedayat, C. Piovera, C. Dallera, A. Gupta, and E. Carpena, A flexible experimental setup for femtosecond time-resolved broad-band ellipsometry and magneto-optics, *Rev. Sci. Instrum.* **86**, 013909 (2015).
- [41] E. Carpena, F. Boschini, H. Hedayat, C. Piovera, C. Dallera, E. Puppini, M. Mansurova, M. Munzenberg, X. Zhang, and A. Gupta, Measurement of the magneto-optical response of Fe and CrO_2 epitaxial films by pump-probe spectroscopy: Evidence for spin-charge separation, *Phys. Rev. B* **87**, 174437 (2013).
- [42] A. Delin, O. Eriksson, B. Johansson, S. Auluck, and J. M. Wills, Calculated magneto-optical properties of cubic and tetragonal Fe, Co, and Ni, *Phys. Rev. B* **60**, 14105 (1999).
- [43] F. Hulliger and E. Pobitschka, On the magnetic behavior of new 2H-NbS_2 -type derivatives, *J. Solid State Chem.* **1**, 117 (1970).
- [44] C.-Y. You and S.-C. Shin, Derivation of simplified analytic formula for magneto-optical Kerr effects, *Appl. Phys. Lett.* **69**, 1315 (1996).
- [45] D. J. Hilton, Ultrafast pump-probe spectroscopy, in *Optical Techniques for Solid-State Characterization*, edited by R. P. Prasankumar and A. J. Taylor (CRC Press, Boca Raton, FL, 2012).
- [46] N. Del Fatti, C. Voisin, M. Achermann, S. Tzortzakis, D. Christofilos, and F. Vallee, Nonequilibrium electron dynamics in noble metals, *Phys. Rev. B* **61**, 16956 (2000).
- [47] P. B. Allen, Theory of Thermal Relaxation of Electrons in Metals, *Phys. Rev. Lett.* **59**, 1460 (1987).
- [48] J. M. E. Harper, T. H. Geballe, and F. J. DiSalvo, Thermal properties of layered transition-metal dichalcogenides at charge-density-wave transitions, *Phys. Rev. B* **15**, 2943 (1977).

- [49] H. J. Zeiger, J. Vidal, T. K. Cheng, E. P. Ippen, G. Dresselhaus, and M. S. Dresselhaus, Theory for dispersive excitation of coherent phonons, *Phys. Rev. B* **45**, 768 (1992).
- [50] S. Ruhman, A. G. Joly, and K. A. Nelson, Coherent molecular vibrational motion observed in the time domain through impulsive stimulated Raman scattering, *IEEE J. Quantum Electron.* **24**, 460 (1988).
- [51] W. G. McMullan and J. C. Irwin, Raman scattering from 2H and 3R-NbS₂, *Solid State Commun.* **45**, 557 (1983).
- [52] A. Laubereau and W. Kaiser, Vibrational dynamics of liquids and solids investigated by picosecond light pulses, *Rev. Mod. Phys.* **50**, 607 (1978).
- [53] S. Fan, S. N. Neal, C. J. Won, J. W. Kim, D. Sapkota, J. J. Yang, D. G. Mandrus, S.-W. Cheong, J. T. Haraldsen, and J. L. Musfeldt, Excitations of intercalated metal monolayers in transition metal dichalcogenides, *Nano Lett.* **21**, 99 (2021).
- [54] T. Pezeril, Laser generation and detection of ultrafast shear acoustic waves in solids and liquids, *Opt. Laser Technol.* **83**, 177 (2016).
- [55] S. Wu, P. Geiser, J. Jun, J. Karpinski, and R. Sobolewski, Femtosecond optical generation and detection of coherent acoustic phonons in GaN single crystals, *Phys. Rev. B* **76**, 085210 (2007).
- [56] M.-C. Lee *et al.*, Direct observation of coherent longitudinal and shear acoustic phonons in the Weyl Semimetal TaAs using ultrafast x-ray diffraction, [arXiv:2011.07196](https://arxiv.org/abs/2011.07196).
- [57] L. Liang, J. Zhang, B. G. Sumpter, Q.-H. Tan, P.-H. Tan, and V. Meunier, Low-frequency shear and layer-breathing modes in Raman scattering of two-dimensional materials, *ACS Nano* **11**, 11777 (2017).
- [58] M. Battiato, K. Carva, and P. M. Oppeneer, Superdiffusive Spin Transport as a Mechanism of Ultrafast Demagnetization, *Phys. Rev. Lett.* **105**, 027203 (2010).
- [59] E. Carpene, E. Mancini, C. Dallera, M. Brenna, E. Puppini, and S. De Silvestri, Dynamics of electron-magnon interaction and ultrafast demagnetization in thin iron films, *Phys. Rev. B* **78**, 174422 (2008).
- [60] B. Koopmans, J. J. M. Ruigrok, F. Dalla Longa, and W. J. M. de Jonge, Unifying Ultrafast Magnetization Dynamics, *Phys. Rev. Lett.* **95**, 267207 (2005).
- [61] C. Stamm, T. Kachel, N. Pontius, R. Mitzner, T. Quast, K. Holldack, S. Khan, C. Lupulescu, E. F. Aziz, M. Wietstruk, H. A. Durr, and W. Eberhardt, Femtosecond modification of electron localization and transfer of angular momentum in nickel, *Nat. Mater.* **6**, 740 (2007).
- [62] C. Dornes, Y. Acremann, M. Savoini, M. Kubli, M. J. Neugebauer, E. Abreu, L. Huber, G. Lantz, C. A. F. Vaz, H. Lemke, E. M. Bothschafter, M. Porer, V. Esposito, L. Rettig, M. Buzzi, A. Alberca, Y. W. Windsor, P. Beaud, U. Staub, D. Zhu *et al.*, The ultrafast Einstein–de Haas effect, *Nature (London)* **565**, 209 (2019).
- [63] R. J. Elliott, Theory of the Effect of Spin-Orbit Coupling of Magnetic Resonance in Some Semiconductors, *Phys. Rev.* **96**, 266 (1954).
- [64] Y. Yafet, *Solid State Physics* (Academic Press, New York, 1963).
- [65] T. Ogasawara, K. Ohgushi, Y. Tomioka, K. S. Takahashi, H. Okamoto, M. Kawasaki, and Y. Tokura, General Features of Photoinduced Spin Dynamics in Ferromagnetic and Ferrimagnetic Compounds, *Phys. Rev. Lett.* **94**, 087202 (2005).
- [66] W. Hubner and K. H. Bennemann, Simple theory for spin-lattice relaxation in metallic rare-earth ferromagnets, *Phys. Rev. B* **53**, 3422 (1996).
- [67] G. M. Muller, J. Walowski, M. Djordjevic, G.-X. Miao, A. Gupta, A. V. Ramos, K. Gehrke, V. Moshnyaga, K. Samwer, J. Schmalhorst, A. Thomas, A. Hutten, G. Reiss, J. S. Moodera, and M. Munzenberg, Spin polarization in half-metals probed by femtosecond spin excitation, *Nat. Mater.* **8**, 56 (2009).
- [68] T. J. Hicken, Z. Hawkhead, M. N. Wilson, B. M. Huddart, A. E. Hall, G. Balakrishnan, F. L. Pratt, S. J. Clark, and T. Lancaster, Energy-gap driven low temperature magnetic and transport properties in Cr_{1/3}MS₂ ($M = \text{Nb}$ or Ta), [arXiv:2105.01393](https://arxiv.org/abs/2105.01393).
- [69] D. Steil, S. Alebrand, T. Roth, M. Krausz, T. Kubota, M. Oogane, Y. Ando, H. C. Schneider, M. Aeschlimann, and M. Cinchetti, Band Structure-Dependent Demagnetization in the Heusler Alloy Co₂Mn_{1-x}Fe_xSi, *Phys. Rev. Lett.* **105**, 217202 (2010).
- [70] C. Guillemard, W. Zhang, G. Malinowski, C. de Melo, J. Gorchon, S. Petit-Watlot, J. Ghanbaja, S. Mangin, P. Le Fevre, F. Betran, and S. Andrieu, Engineering Co₂MnAl_xSi_{1-x} Heusler compounds as a model system to correlate spin polarization, intrinsic Gilbert damping, and ultrafast demagnetization, *Adv. Mater.* **32**, 1908357 (2020).
- [71] S. Pan, T. Seki, K. Takanashi, and A. Barman, Ultrafast demagnetization mechanism in half-metallic Heusler alloy thin films controlled by Fermi level, *Phys. Rev. B* **101**, 224412 (2020).
- [72] M. Battiato, J. Minar, W. Wang, W. Ndiaye, M. C. Richter, O. Heckmann, J.-M. Mariot, F. Parmigiani, K. Hricovini, and C. Cacho, Distinctive Picosecond Spin Polarized Dynamics in Bulk Half Metals, *Phys. Rev. Lett.* **121**, 077205 (2018).
- [73] M. Dressel and G. Grüner, *Electrodynamics of Solids* (Cambridge University Press, Cambridge, UK, 2002).
- [74] H. Ibach and H. Lüth, *Solid-State Physics* (Springer, Berlin, 2009).
- [75] Q. Peng, Z. Wang, B. Sa, B. Wu, and Z. Sun, Blue phosphorene/MS₂ ($M = \text{Nb}$, Ta) heterostructures as promising flexible anodes for lithium-ion batteries, *ACS Appl. Mater. Interfaces* **8**, 13449 (2016).
- [76] A. C. Bornstein, B. J. Chapman, N. J. Ghimire, D. G. Mandrus, D. S. Parker, and M. Lee, Out-of-plane spin-orientation dependent magnetotransport properties in the anisotropic helimagnet Cr_{1/3}NbS₂, *Phys. Rev. B* **91**, 184401 (2015).